



Hydrogen bonding-mediated phase-transition gelatin-based bioadhesives to regulate immune microenvironment for diabetic wound healing

Zhuoling Tian^{a,b,c}, Ruoheng Gu^b, Wenyue Xie^b, Xing Su^b, Zuoying Yuan^b, Zhuo Wan^b, Hao Wang^b, Yaqian Liu^{b,d}, Yuting Feng^b, Xiaozhi Liu^e, Jianyong Huang^{b,c,*} 

^a Academy for Advanced Interdisciplinary Studies, Peking University, Beijing, 100871, China

^b Department of Mechanics and Engineering Science, College of Engineering, Peking University, Beijing, 100871, China

^c Nanchang Innovation Institute, Peking University, Nanchang, 330096, China

^d College of Science, Inner Mongolia University of Technology, Hohhot, 010051, China

^e Tianjin Key Laboratory of Epigenetics for Organ Development of Premature Infants, Fifth Central Hospital of Tianjin, Tianjin, 300450, China

ARTICLE INFO

Keywords:

Injectable gelatin
Phase transition
Bioadhesives
Immune microenvironment
Diabetic wound healing

ABSTRACT

Gelatin-based biomaterials have emerged as promising candidates for bioadhesives due to their biodegradability and biocompatibility. However, they often face limitations due to the uncontrollable phase transition of gelatin, which is dominated by hydrogen bonds between peptide chains. Here, we developed controllable phase transition gelatin-based (CPTG) bioadhesives by regulating the dynamic balance of hydrogen bonds between the peptide chains using 2-hydroxyethylurea (HU) and punicalagin (PA). These CPTG bioadhesives exhibited significant enhancements in adhesion energy and injectability even at 4 °C compared to traditional gelatin bioadhesives. The developed bioadhesives could achieve self-reinforcing interfacial adhesion upon contact with moist wound tissues. This effect was attributed to HU diffusion, which disrupted the dynamic balance of hydrogen bonds and therefore induced a localized structural densification. This process was further facilitated by the presence of pyrogallol from PA. Furthermore, the CPTG bioadhesive could modulate the immune microenvironment, offering antibacterial, antioxidant, and immune-adjustable properties, thereby accelerating diabetic wound healing, as confirmed in a diabetic wound rat model. This proposed design strategy is not only crucial for developing controllable phase-transition bioadhesives for diverse applications, but also paves the way for broadening the potential applications of gelatin-based biomaterials.

1. Introduction

Due to excellent biocompatibility and biodegradability, gelatin [1] has been widely utilized in a larger number of fields like biosensors [2], soft robotics [3], wearable [4] and implantable electronics [5], three-dimensional (3D) printing [6], biomedicine [7,8] and tissue engineering [9]. However, its uncontrollable phase transition compromises its properties [10–12], particularly in terms of injectability and adhesiveness, significantly limiting its potential applications. As the temperature gradually decreases, the peptides in gelatin usually transition from a random coil state to a left-handed helix [13]. The adjacent left-handed helices then form a right-handed superhelical structure through hydrogen bonding, creating crosslinking points [14]. In gelatin-based bioadhesives, an increase in crosslinking points causes the

gelatin sol to gradually transform into a gel, leading to increased stiffness and brittleness [10,15]. Furthermore, as crosslinking points increase, the gelatin network becomes tighter, reducing the number of exposed adhesive groups and thereby weakening the adhesion strength and stability to a certain extent [12,16]. Additionally, environmental factors such as ionic strength [17], pH and solvents [18] can also exert an crucial impact on the gelatin-based bioadhesives.

Generally, the imbalance in the inflammatory response is a critical factor impeding the healing of diabetic wounds [19]. Elevated systemic blood glucose levels lead to excessive protein glycosylation, resulting in the formation of advanced glycation end products. This, in turn, activates the immune system, causing the recruitment of excessive inflammatory cytokines and infiltrating immune cells [20]. The inflammatory environment particularly hinders the transition of pro-inflammatory M1

Peer review under the responsibility of KeAi Communications Co., Ltd.

* Corresponding author. Department of Mechanics and Engineering Science, College of Engineering, Peking University, Beijing, 100871, China.

E-mail address: jyhuang@pku.edu.cn (J. Huang).

<https://doi.org/10.1016/j.bioactmat.2024.12.014>

Received 12 October 2024; Received in revised form 14 December 2024; Accepted 16 December 2024

2452-199X/. 2024 The Authors. Publishing services by Elsevier B.V. on behalf of KeAi Communications Co. Ltd. This is an open access article under the CC BY-NC-ND license (<http://creativecommons.org/licenses/by-nc-nd/4.0/>).

macrophages to pro-healing M2 macrophages [21]. This dysregulation of the immune microenvironment inhibits the proliferation of endothelial cells, fibroblasts, and keratinocytes, and thereby hampers re-epithelialization and angiogenesis, which severely impedes diabetic wound healing. To this end, strategies targeting the regulation of the immune microenvironment and promoting M2 macrophage polarization have been proposed as effective methods to enhance the healing of diabetic wounds [22,23]. In recent years, biocompatible hydrogels and bioadhesives with immunomodulatory properties have been explored for applications in diabetic wound healing [24–27]. However, the incorporation of bioactive compositions, such as cytokines, stem cells, and engineered nanoparticles, poses considerable challenges related to therapeutic costs and scalability for clinical translation [28].

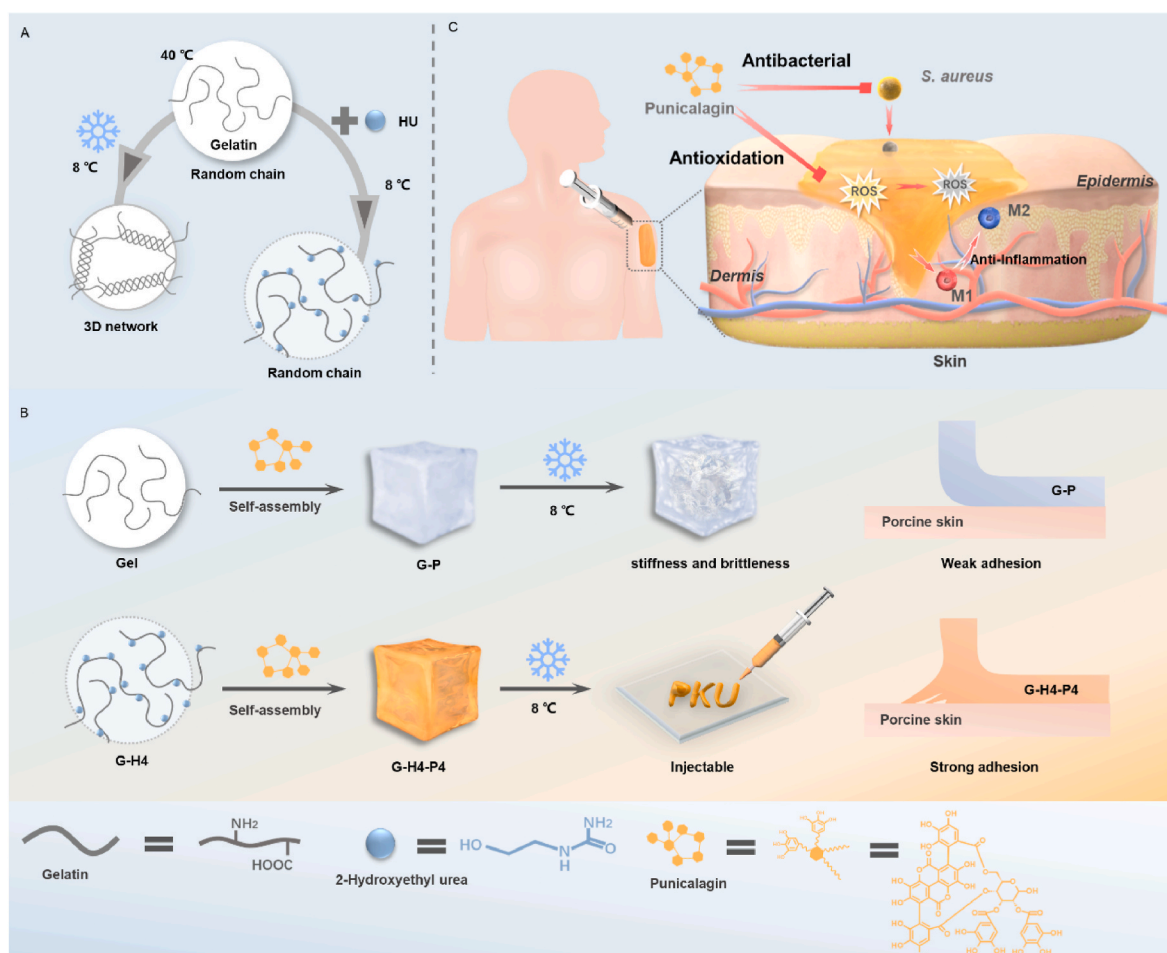
Here, we develop controllable phase-transition gelatin-based (CPTG) bioadhesives mainly composed of gelatin, 2-hydroxyethylurea (HU) and punicalagin (PA), where the hydrogen bond dominated self-crosslinking of gelatin and the resultant phase transition are controllably inhibited by allowing the specific functional molecules including HU and PA, to interact with the peptides in gelatin. Essentially, HU can disrupt the hydrogen bonds between gelatin molecules, thereby modulating the phase transition of gelatin at different temperatures (Scheme 1A). Meanwhile, PA may form additional hydrogen bonds with gelatin, enhancing its adhesion strength to biological tissues. In comparison to traditional gelatin-based bioadhesives, the developed CPTG bioadhesive

can achieve significant enhancements in adhesion energy and injectability at temperatures as low as 8 °C (Scheme 1B), due to the effective inhibition of hydrogen bonding between gelatin molecules. Once the bioadhesive contacts moist wound tissues, the HU molecules, acting as hydrogen bond de-crosslinking agents, can diffuse out of the bioadhesive. This disrupts the dynamic balance of hydrogen bonds between gelatin molecules, leading to localized strengthening in the gelatin-based bioadhesive with the aid of pyrogallol from PA, thereby forming self-reinforcing interfacial adhesion to the wound tissues. We also demonstrate that the developed CPTG bioadhesives possess the ability to modulate the immune microenvironment for diabetic wound healing (Scheme 1C), as confirmed in an *in vivo* diabetic rat model.

2. Materials and methods

2.1. Materials

Gelatin (GE, purity: BR) and 2-Hydroxyethylurea (HU, purity > 95%) were purchased from Shanghai Yuanye Bio-Technology Co., Ltd. Punicalagins (PA, chemical formula: $C_{48}H_{28}O_{30}$, purity > 40%) was supplied by Beijing Feimo Bio life science Co., Phosphate Buffer Saline (PBS, pH = 7.4) and Dulbecco's Modified Eagle's medium (DMEM) were derived from Thermo Fisher Scientific. RPMI 1640 medium and fetal bovine serum (FBS) were purchased from Gibco. All chemicals were used as



Scheme 1. Design and fabrication of controllable phase-transition gelatin-based (CPTG) bioadhesives to regulate immune microenvironment for diabetic wound healing. (A) Schematic diagram illustrating the regulatory effect of the HU molecules on the hydrogen bonds formed between gelatin peptide chains. The HU molecules could disrupt the formation of intrinsic hydrogen bonds between gelatin peptides, thereby altering their phase transition temperature. (B) Comparison of mechanical properties and interfacial adhesion capabilities between traditional gelatin-based bioadhesive and the newly developed G-H4-P4 bioadhesive at 8 °C. The traditional gelatin based bioadhesive was brittle and exhibited weak adhesion, whereas the G-H4-P4 bioadhesive demonstrated injectability and strong adhesion. (C) Schematic representation illustrating the application of the CPTG bioadhesives in the healing process of diabetic wounds.

received.

2.2. Fabrication of the G-Hx solution and sol-gel transition analysis of gelatin

2-Hydroxyethylurea (HU) was dissolved in deionized water to prepare a buffer, which was then used to dissolve gelatin, creating a gelatin solution with a mass fraction of 10%. The detailed compositions of the G-Hx solution are listed in Table S1, where “x” denotes 0, 1, 2, 3, 4, respectively. The relationship between the phase-transition temperature (i.e., sol-gel transition temperature T_{gel}) of gelatin and the HU content was determined using the G' - G'' crossover temperature method [29]. The G-Hx solutions were loaded into a rotary rheometer (Anton Paar, MCR302), and dynamic temperature sweep measurements were conducted. The solutions were equilibrated at 40 °C for 10 min between the plates. Subsequently, the temperature was ramped from 40 °C to 10 °C at a rate of 2 °C min⁻¹, with a frequency of 10 rad s⁻¹ and a torque of 70 μNm. In the experiments, T_{gel} was defined as the temperature at which $G' = G''$.

2.3. Molecular dynamics simulation of G-Hx solution

Molecular dynamics simulation was carried out by using LAMMPS. The triple helix structure of gelatin was obtained from the Protein Data Bank (Protein Data Bank (PDB) entry 1cgd [30]). CHARMM-GUI [31] were utilized to construct implicit solvent models of Gel and G-H with periodic boundary conditions (PBCs). For Gel, energy minimization was performed using conjugate gradient algorithm until the energy convergence accuracy was less than 1e⁻⁸ kcal/mol. The model was equilibrated at 273, 278, 283, 288, 293, 298, 303, 308 K at 10 ns in the canonical ensemble. For G-H, additional 95 HU molecules were placed in the simulation box, and the system was relaxed in the isothermal-isobaric ensemble at 303 K for 200 ps before being treated with the same approach as described above. During the simulations, the CHARMM36m [32] force field was employed to determine the atomic interactions between gelatin, water and hydroxyethyl urea molecules. The temperature and pressure of the system were controlled using the Nosé-Hoover6 thermostat and barostat. Electrostatic interactions and van der Waals forces were computed based on the particle-particle particle-mesh (PPPM) method [33] and Lennard-Jones potential, respectively. The Tip3p water model was used to describe the interactions between water molecules, with constraints applied to specified bonds and angles of water during the molecular dynamics [34]. The time step was set to 1 fs. The model structure was provided in this paper using the Visual Molecular Dynamics (VMD) software [35]. The radius of gyration of gelatin was estimated to analyse the compactness of the three chains based on the expression

$$R_g = \sqrt{\frac{\sum_i m_i (\mathbf{r}_i - \mathbf{r}_c)^2}{\sum_j m_j}} \quad (1)$$

where, i denotes the atomic number, \mathbf{r}_i represents the coordinates of atom i , and \mathbf{r}_c corresponds to the coordinates of the centroid of the gelatin chain. The radius of gyration was calculated every 2 ps during the last 1 ns of the simulation, and the average value was obtained to ensure the accuracy of the results. The interaction energy among the three gelatin chains was calculated via the following formula

$$E_{\text{interaction energy}} = E_{\text{total}} - E_{\text{chain A}} - E_{\text{chain B}} - E_{\text{chain C}} \quad (2)$$

where $E_{\text{interaction energy}}$ represents the interaction energy among the three gelatin chains, E_{total} denotes the energy of gelatin; $E_{\text{chain A}}$, $E_{\text{chain B}}$ and $E_{\text{chain C}}$ are the energies of individual chains A, B and C, respectively. For the hydrogen bond statistics, we assumed that a hydrogen bond was formed if an atom with a bonded hydrogen (the donor, D) and another

atom (the acceptor, A) had a D-A distance of less than 3.5 Å and a D-H-A angle of less than 30° [36].

2.4. Synthesis of the G-P/G-H4-Py bioadhesives

To prepare the G-P bioadhesive, 10% (w/v) gelatin was dissolved in deionized water, followed by the direct addition of 10% (w/v) PA. After stirring for 30 s, the precipitated material was collected as the G-P bioadhesive. For the synthesis of G-H4-Py bioadhesives, gelatin was dissolved in a 3.84 mol L⁻¹ HU solution at a concentration of 10% (w/v). This solution was then mixed with varying amounts of punicalagin (PA). After stirring for 30 s, the precipitates formed were collected as the G-H4-Py bioadhesives. The detailed compositions of the G-P and G-H4-Py bioadhesives are listed in Table S2, where “y” denotes 0, 1, 2, 3, and 4, respectively.

2.5. Characterization of the G-P/G-H4-Py bioadhesives

2.5.1. Fourier transform infrared spectroscopy (FTIR)

The hydrogen bonding interactions between G-Hx and the formation of G-H4-Py bioadhesives were characterized using Fourier transform infrared (FTIR) spectroscopy (Bruker Tensor 27 FTIR spectrometer) [37]. Each spectrum was obtained by averaging 16 scans over a wave-number range from 4000 to 400 cm⁻¹ with a resolution of 2 cm⁻¹.

2.5.2. ¹H NMR

The hydrogen bonding interactions between HU and Gel were characterized by ¹H solution-state NMR spectra (Bruker Avance III HD 500Hz) in D₂O at 287 K [38]. A solid-state NMR was carried out to clarify the molecular interactions between HU, PA, and gelatin (Bruker Avance Neo 400WB).

2.5.3. Scanning electron microscopy (SEM)

The lyophilized bioadhesive samples were coated with gold and analyzed using a TESCAN MAIA3 ultra high-resolution field emission scanning electron microscope (SEM) at an acceleration voltage of 5 kV to observe the structure of the bioadhesive networks [37].

2.5.4. Mechanical properties

The mechanical properties of the bioadhesives were characterized using a rotary rheometer (Anton Paar, MCR302) in frequency sweep mode, ranging from 0.1 to 100 Hz with a 5.0% strain amplitude at 25 °C.

2.5.5. Self-healing properties

An alternate step strain sweep test was conducted to evaluate the self-healing capacity of the bioadhesive. The storage modulus (G') and loss modulus (G'') of the G-H4-P4 bioadhesive were measured at 25 °C with a frequency of 10 rad s⁻¹. The measurements were taken over three cycles, alternating between a small oscillation strain ($\gamma = 5.0\%$) and a large oscillation strain ($\gamma = 400\%$), ensuring a duration of 200 s for each strain value.

2.5.6. Injectability assessment

To investigate the injectable properties of G-P and G-H4-P4 bioadhesives at low temperatures, the linear viscosity (η) was measured under frequency sweep mode.

2.5.7. Adhesiveness evaluation

The adhesion strengths of the bioadhesives to biological tissues, including dry or wet fresh porcine skin, stomach, liver, and colon, were quantified using a lap-shear test at room temperature (RT) [39]. The bioadhesive was applied between two tissue slides, each measuring 30 mm in length and 5 mm in width. After pressing for 10 s, the lap-shear test was conducted on an STS10N tensometer (Xiamen East Instrument Co. Ltd.) at a speed of 5 mm min⁻¹. The contact area between the two tissue pieces bonded by the bioadhesive was measured with a ruler,

ranging from 10 to 100 mm². The effect of temperature on adhesive energy was evaluated by the T-peeling test [7] and lap-shear test at 4, 25 and 37 °C, respectively. To assess the impact of water on adhesive behaviour, the prepared testing samples were washed with 20 mL of distilled water using a dropper.

2.5.8. Hydrogel degradation

The *in vitro* degradation of the bioadhesives was examined by placing the bioadhesives in 30 mL PBS and incubated in a 37 °C shaker [7]. At each time interval, the dry weights were measured.

2.6. Evaluation of HU and PA diffusion

HU solutions of varying concentrations (0.5, 2.5, 5, 10, and 20 µg mL⁻¹) and PA solutions of varying concentrations (6.125, 12.5, 25, 50, and 100 µg mL⁻¹) were prepared with deionized water. To obtain the standard curve of HU, high-performance liquid chromatography (HPLC) was performed using a 1260 Infinity II system (Agilent, USA) with a 120 EC-C18 column (Agilent, USA). The eluent was ultra-pure water, and the analysis was conducted under isocratic conditions at room temperature (RT) with a flow rate of 0.8 mL min⁻¹ and an injection volume of 10 µL. The detection wavelength was set at 194 nm. For PA, the standard curve was obtained using HPLC with gradient elution (0–15 min, 95% A; 15–17 min, 70% A; 17–18 min, 95% A). The mobile phase consisted of 0.2% phosphoric acid aqueous solution (mobile phase A) and 0.1% acetonitrile (mobile phase B). The detection wavelength was set at 258.7 nm. For the actual diffusion measurements, a G-H4-P4 bioadhesive column with a diameter of 6 mm and a height of 3 mm was placed in 40 mL of deionized water. Samples of 1 mL were collected at different time intervals and analyzed using HPLC. The concentrations of HU and PA were determined at these intervals by referencing the respective standard curves.

2.7. *In vitro* experiments

2.7.1. Cell biocompatibility and hemocompatibility

Cell counting kit-8 (CCK-8, Bimake) and live/dead assays (Invitrogen) [39] were employed to evaluate the cytotoxicity of the bioadhesives. To this end, L929 cells were cultured in RPMI 1640 medium supplemented with 10% FBS and 1% penicillin-streptomycin in a CO₂ incubator at 37 °C. The cells were then seeded into 96-well plates at a density of 1.5 × 10³ cells/well and incubated with extracts of the G-H4-Py bioadhesive. For the CCK-8 assay, the extracts were removed, and fresh medium containing 10% CCK-8 reagent was added. Absorbance was measured at 450 nm using a Multiskan FC Microplate Reader (Thermo, USA). For the Live/Dead staining, cells were incubated with 2 µM calcein AM (live) in DPBS and 4 µM EthD-1 (dead) working solution in the dark. The morphologies of the samples were observed using a laser scanning confocal microscope (Nikon, Japan).

The hemocompatibility of the bioadhesives was assessed by incubating rat red blood cells (RBCs) with G-H4-Py bioadhesives [40]. Specifically, purified RBCs were suspended in 50 mL of phosphate-buffered saline (PBS). Bioadhesive extracts, distilled water, and normal saline (NS) were then added to the RBC suspension in a ratio of 1:1. The absorbance was then measured at 540 nm through a Multiskan FC Microplate Reader (Thermo, US).

2.7.2. *In vitro* model of diabetes and RNA-Seq analysis

RAW 264.7 cells were cultured in high glucose DMEM supplemented with 10% FBS in a CO₂ incubator at 37 °C. Cells were seeded at a density of 1 × 10⁴ cells per well in a 24-well plate and cultured for 24 h with lipopolysaccharide (LPS) treatment to simulate *in vitro* diabetes (LPS group). Following incubation with the bioadhesive extract for 24 h, cells were lysed using Trizol buffer. Total RNA was extracted and purified, followed by reverse transcription to cDNA. The amplified and enriched cDNA was then analyzed based on the Illumina NGS platform.

2.7.3. Antibacterial activity of the bioadhesives

The antibacterial properties of the G-H4-P4 bioadhesives were evaluated using the colony-forming unit (CFU) counting method [41]. Both Gram-negative bacteria (*E. coli*) and Gram-positive bacteria (*S. aureus*) served as bacterial models. A bacterial suspension (PBS, OD₆₀₀ = 0.5) was mixed with the bioadhesive extract, while an equal volume of sterile PBS was used as a blank control. After incubation for 24 h at 37 °C, the CFUs on the Petri dishes were counted to quantitatively assess the antibacterial efficacy.

2.7.4. Antioxidant efficiency of the bioadhesives

The *in vitro* antioxidant efficiency of the bioadhesives was evaluated using the 2,2-diphenyl-1-picrylhydrazyl (DPPH) free radical scavenging assay (Shanghai Yuanye Bio-Technology Co.) [42]. DPPH and various G-H4-Py bioadhesives were each dissolved in ethanol. The mixtures were stirred and incubated in the dark. Absorbance was measured at 517 nm. A reactive oxygen species (ROS) assay kit (Yeasten) was employed to investigate the intracellular ROS scavenging ability of the bioadhesive. RAW264.7 (5 × 10⁵ cells/well) were seeded in a 24-well plate. The cells were then treated with a ROS-up reagent (working solution, 100 µM) and DMEM without FBS, serving as positive and negative controls, respectively. The experimental group was treated with the bioadhesive extract containing 100 µM ROS-up reagent. After incubation, the oxidant-sensing probe 2',7'-dichlorodihydrofluorescein diacetate (DCFH-DA, 10 µM) was added. The intracellular ROS levels were observed by a laser scanning confocal microscope (Nikon, Japan).

2.7.5. Evaluation of immune microenvironment modulation

In vitro immunomodulatory assessment was performed using morphological analysis, fluorescence-activated cell sorter (FACS), immunofluorescence staining, and RT-PCR [43]. RAW 264.7 cells were seeded in a 24-well plate and incubated with LPS for 24 h to (hereafter referred to as the LPS group). Subsequently, the cells were treated with extracts from the G-H4-Py bioadhesives, which were designated as the LPS + G-H4-Py groups. To visualize cell morphological changes, cells were fixed with 4% paraformaldehyde and stained with phalloidin for F-actin and 4',6-diamidino-2-phenylindole (DAPI) for nuclei. Morphologies were observed using a laser scanning confocal microscope (Nikon, Japan). Ten random cells from each group were selected to quantify the average area using the ImageJ software (National Institutes of Health, Bethesda, MD, USA).

For the FACS analysis, cells were fixed, permeabilized, and blocked, followed by incubation with primary antibody CD206 and Alexa Fluor 488-conjugated secondary antibody (Abcam). For the iNOS staining, Alexa Fluor 594-conjugated iNOS antibody (Biolegend) was used. After washing, cells were stored at 4 °C for the subsequent FACS analysis. For the immunofluorescence analysis, cells were fixed, permeabilized, and blocked, then incubated overnight with primary antibody CD206 (Abcam) and subsequently with Alexa Fluor 488-conjugated secondary antibody (Abcam). For the iNOS staining, Alexa Fluor 594-conjugated iNOS antibody was incubated with the cells overnight at 4 °C. DAPI was used to stain the cell nuclei. The stained cell samples were imaged with a laser scanning confocal microscope (Nikon, Japan).

For the RT-PCR analysis, total RNA was extracted using the RNA-Quick Purification Kit (Shanghai Yishan Bio-Technology Co.) and reverse-transcribed with PrimeScript RT Master Mix (Takara). Gene expression was quantified using SYBR Premix Ex Taq (Takara) on a Bio-Rad RT-PCR system (Bio-Rad). Glyceraldehyde-3-phosphate dehydrogenase (GAPDH) was used as the housekeeping gene. M1 markers included iNOS and IL-1β, while M2 markers included CD206 and Arg-1. Primer sequences and specific qRT-PCR steps were listed in Table S2. Relative gene expression levels were normalized to the GAPDH level by means of the ΔΔCt method [44].

2.8. In vivo experiments

2.8.1. Diabetic wound healing assessment

Eight-week-old female SD rats were acclimated for one week. The type I diabetic rat model was established as previously described [41]. Briefly, the rats were fed with a high-fat, high-sugar diet for 2 weeks, followed by intraperitoneal injections of streptozotocin (50 mg kg^{-1}) after a 12-h fast for five consecutive days. The glucose levels of STZ-treated rats were monitored using a glucometer (Yuwell, China). The induction was considered successful when fasting blood glucose levels consistently exceeded 300 mg dL^{-1} (16.7 mmol L^{-1}) for 2 weeks. The rats were anesthetized with isoflurane (5% for induction and 1.5–2.5% for maintenance) and shaved in preparation for surgery. Full-thickness wounds were created on the shaved back with 12 mm biopsy punches. The wounds were treated with the pre-sterilized G-H4-P4 bioadhesive, Tegaderm™ film, or left untreated ($n = 3$). The wound areas were photographed with a digital camera on days 1, 3, 5, 7, 10, and 14 post-surgery, with a ruler used as a reference. The corresponding wound closure areas were quantified using the ImageJ software.

2.8.2. Histological analysis and immunofluorescence staining

Animals were euthanized using carbon dioxide on days 3, 7, and 14 for analyses of inflammation, fibroblast-to-myofibroblast conversion, and tissue or blood vessel regeneration, respectively [41]. The wound tissues were fixed, embedded, and sectioned for subsequent procedures. Sections from day 14 were deparaffinized, rehydrated, and stained with hematoxylin and eosin (H&E) and Masson's Trichrome (MST). For the immunofluorescence staining, goat serum was employed to block non-specific binding. To detect myofibroblasts, we adopted a rabbit anti- α -SMA primary antibody (1:500, KALANG, KL-0189R) and a goat anti-rabbit IgG/TRITC secondary antibody (1:1000, ZSGB, Beijing, China). For the angiogenesis detection, we utilized a rabbit anti-CD31 primary antibody (1:400, SMN, Wuhan, China) and a goat anti-rabbit IgG/TRITC secondary antibody (1:1000, ZSGB, Beijing, China). Sections from day 3 were selected to monitor the inflammatory environment. For the macrophage detection, we used a mouse anti-F4/80 primary antibody (1:200, Bioss, Beijing, China) and a goat anti-mouse IgG/FITC secondary antibody (1:1000, ZSGB, Beijing, China). M1 macrophages were identified with a rabbit anti-iNOS primary antibody (1:500, Abcam) and a goat anti-rabbit IgG/TRITC secondary antibody (1:1000, ZSGB, Beijing, China). M2 macrophages were identified with a rabbit anti-CD163 primary antibody (1:400, Bioss, Beijing, China) and a goat anti-rabbit IgG/TRITC secondary antibody (1:1000, ZSGB, Beijing, China). Cell nuclei were stained with DAPI. Immunohistochemical staining was carried out to evaluate the expression levels of cytokines, including IL-1 β , TNF- α , Arg-1 and IL-10. The slides were imaged with a pathology panoramic scanner (3DHISTECH), and the corresponding quantitative analysis was carried out using the ImageJ software.

2.9. Statistical analysis

Statistical analysis was conducted using the Origin 2018 software. Data from at least three independent experiments were expressed as Mean \pm Standard Deviation (SD). One-way ANOVA was adopted for pairwise comparisons. The p values ($p < 0.05$) were considered statistically significant. The $p \leq 0.05$ was considered statistically significant and denoted by *, while $p \leq 0.01$ was denoted by ** in our statistical analysis.

3. Results and discussion

3.1. Design and preparation of the CPTG bioadhesives

The essence of achieving controllable phase transitions in gelatin-based biomaterials lies in diminishing hydrogen-bond interactions

between gelatin molecules, thereby effectively preventing self-crosslinking induced by environmental temperatures. To this end, we first introduced the HU molecules to disrupt the hydrogen bonds between gelatin molecules because it could form hydrogen bonds with the amino and carbonyl groups in gelatin molecules, therefore occupying the self-crosslinking sites (Scheme 1A). Our rheological data revealed a significant decrease in the phase-transition temperature T_{gel} with increasing the HU concentration. Notably, when the weight ratio of gelatin to HU reached 1:4 (hereafter referred to as G-H4), the phase-transition temperature dropped to 8°C (Fig. 1A). Fig. S1A showed the sol-gel states of the prepared “G-Hx” bioadhesives at various temperatures, whose compositions were listed in Table S1 with “x” denoting 0, 1, 2, 3, and 4, respectively, in the “G-Hx” bioadhesives. As shown in the Fourier Transform Infrared (FTIR) analysis (Fig. 1B), peaks near 3320 cm^{-1} are characteristic of hydroxyl and amine groups in gelatin [45]. In the groups of G-H2 and G-H4, the peak shifted to a lower wavenumber, which indicated the formation of additional hydrogen bonds. Furthermore, the peaks of the pure gelatin solution (Gel) and the G-H2 group in the amide I band are above 1650 cm^{-1} (triple helix, intramolecular H-bonds), while the peak for G-H4 is at 1648 cm^{-1} (random coil and solvent-Gly H-bonds) [46]. The ^1H NMR spectra of G-H4 revealed characteristic peaks corresponding to the -OH groups of HU (~ 4.42 ppm) and the C-H protons (~ 7.72 ppm and 7.18 ppm) on the benzene ring of Gel. In addition, the ^1H NMR signal for the -OH group in HU displayed a downfield shift, while the ^1H NMR signal for Gel shifted to a lower frequency (Fig. S2C). These findings confirm that a high content of HU interacts with gelatin through hydrogen bonds, preventing self-crosslinking of gelatin and thus modulating its phase transition at different temperatures (Fig. 1C).

We subsequently employed molecular dynamic (MD) simulations to investigate the hydrogen bonding interactions between HU and gelatin molecular chains (Fig. 1D). To this end, we created the triple helix structures in gelatin in both the absence and presence of HU to quantify the hydrogen bonding interactions modulated by HU (Fig. 1E). The molecular conformations of gelatin and the corresponding G-Hx bioadhesive were presented, with the maximum diameters of the gelatin triple helix structure measured at 283 K . The addition of HU was observed to expand the maximum diameters of gelatin from 13.85 \AA to 16.08 \AA . Concurrently, the gyration radius of gelatin increased from 24.07 to 34.09 \AA (Fig. 1F). These suggest that HU occupies the hydrogen-bonding sites responsible for gelatin self-crosslinking, resulting in a looser gelatin structure and preventing its renaturation. Moreover, the interaction energy between the three chains of gelatin in the G-Hx model was -272.79 kcal/mol , significantly higher than that in the Gel model (Fig. 1F and Fig. S1B). This demonstrates that the introduction of HU destabilizes the triple helix structure of the gelatin chains. Likewise, Fig. 1G shows that numerous hydrogen bonds were formed between N-H (Gly) and C=O (Xaa, other amino acid residues) in the Gel model. In contrast, some of these bonds were replaced by N-H (Gly) and C=O (HU) in the G-H model, leading to a random coil structure. This finding is consistent with the FTIR spectra results (Fig. 1B).

The natural polyphenol macromolecule punicalagin (PA), known for its diverse biological activities, was utilized to enhance binding with gelatin through hydrogen bonds and dynamic chemical bonds [47], which contributed to the formation of the CPTG bioadhesives (Fig. 2A and Fig. S2A). The ^1H NMR signal of G-H4-P4 exhibited an upfield shift relative to G-P, suggesting that the addition of HU competed with PA and disrupted the hydrogen bonding interactions between gelatin and PA (Fig. S2G). Also, PA exhibited a range of biological activities, such as modulating the immune microenvironment [48]. In this study, PA reacted adequately when the weight ratio of PA to G was at least 2:1 (Figs. S2B and S2D). As the PA content increased, the cross-linking density increased, resulting in a more tightly knit network (Figs. S2E and S2F), as confirmed by the SEM analysis. Consequently, once PA saturation was reached, the total weight of the G-H4-Py bioadhesives increased less than the weight of the added PA. Therefore, PA to gelatin

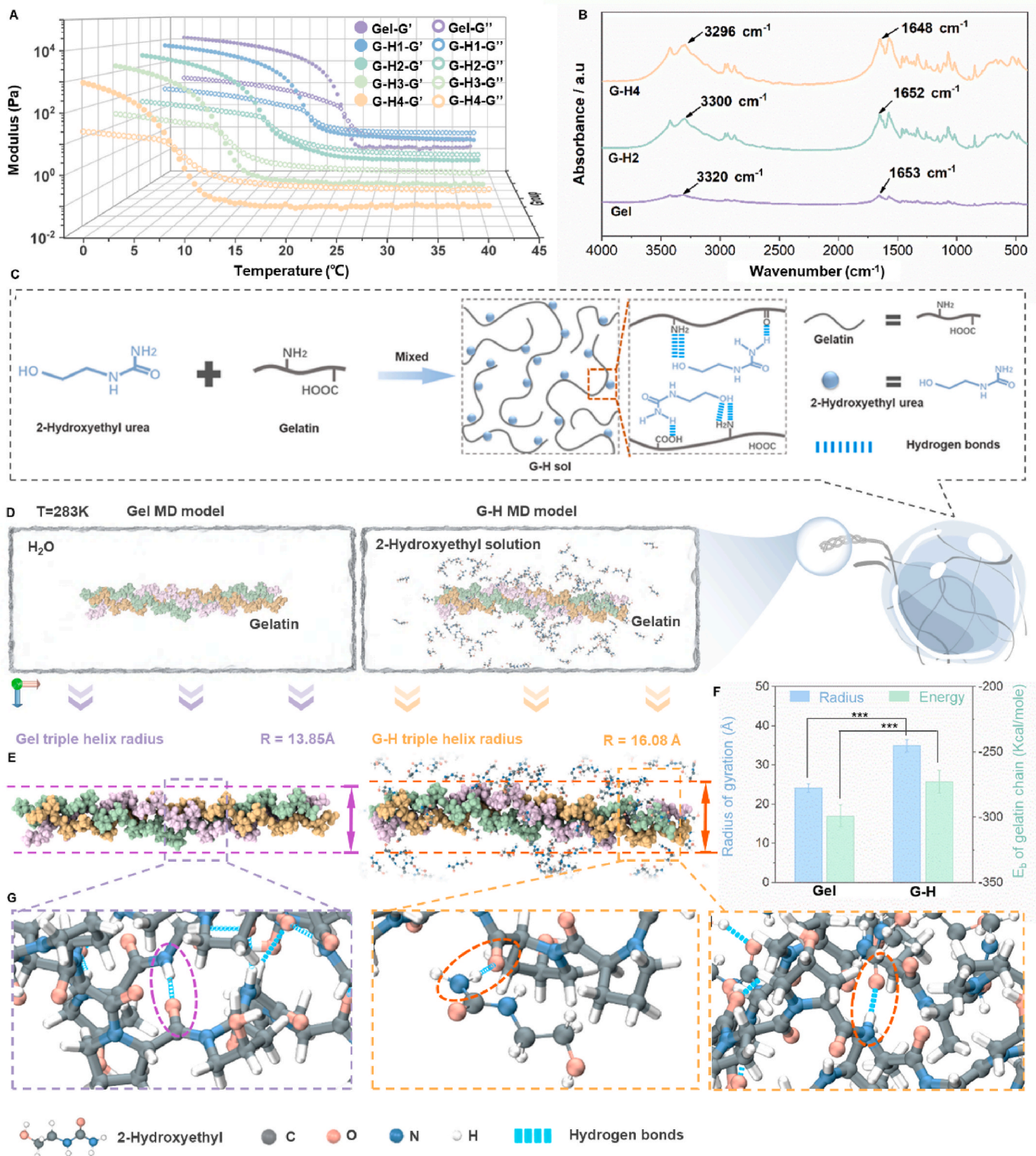


Fig. 1. Dependence of gelatin's phase-transition temperature on HU content at various temperatures. (A) Plots of modulus versus temperature for the G-Hx bioadhesives (where x equals 0, 1, 2, 3, and 4, respectively). The gelation temperature (T_{gel}) was defined as the temperature at which the storage modulus (G') equals the loss modulus (G''). (B) The FTIR spectra for the G-Hx bioadhesives (where x equals 0, 2, and 4, respectively). (C) Schematic illustration of the hydrogen bonding interactions between HU and gelatin molecular chains at 40 °C. (D) Molecular dynamics simulation snapshot depicting the atomic-level interactions within system. (E) Molecular dynamics simulation results delineated the triple helix structures in gelatin in both the absence and presence of HU. (F) Molecular dynamics simulations presented the interaction energy between gelatin chains and the radius of gyration of gelatin at 283 K. (G) Molecular dynamics simulations depicted the hydrogen bonding interactions in gelatin, both in the absence and presence of HU.

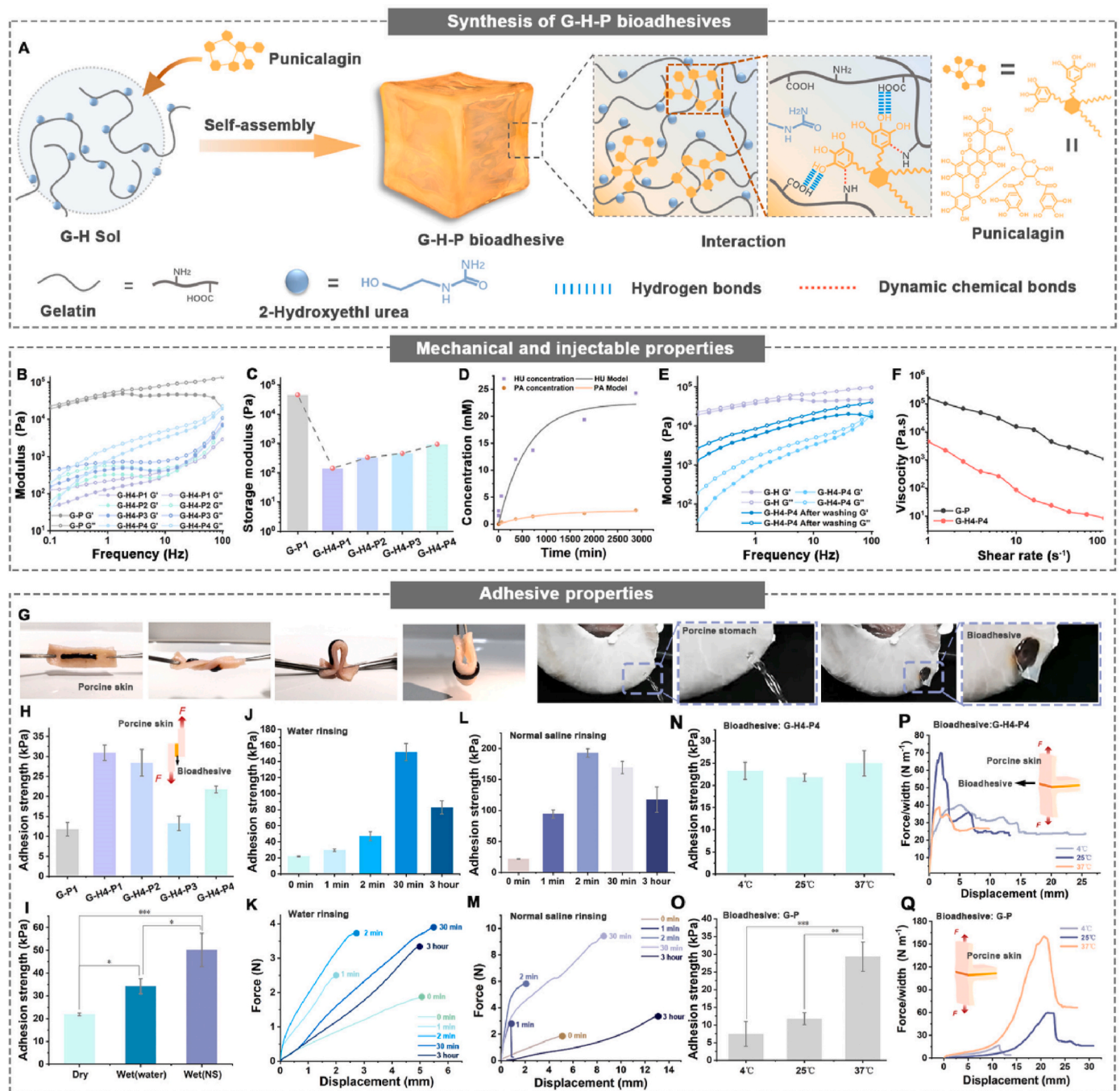


Fig. 2. Characterization of mechanical properties, injection and adhesion properties of the developed CPTG bioadhesives. (A) Synthesis of the G-H4-Py bioadhesives. (B) Rheological analysis of the G-Hx-Py bioadhesives in the frequency sweep mode (where $x = 0$, and 4 and $y = 1, 2, 3$, and 4 , respectively, in the “G-Hx-Py” bioadhesives). (C) Storage modulus at 1 Hz for the G-Hx-Py bioadhesives. (D) Diffusion of HU and PA in water. The bioadhesive samples were soaked in 40 mL of pure water at room temperature to monitor the diffusion of HU and PA into the surrounding water over time. Experimental data are represented as dots, while the release curves are fitted. (E) Changes in the storage modulus of the G-H4-P4 bioadhesive before and after washing with water. (F) Shear-thinning tests of the bioadhesives at 4 °C. (G) Stability of the G-H4-P4 bioadhesive adhesion on porcine skin after stretching, twisting, and bending the skin. Sealing of a fluid-leaking ex vivo porcine stomach using a film adhered with G-H4-P4 bioadhesive. (H) Average adhesion strength of the G-P1 and G-H4-Py ($y = 1, 2, 3$, and 4) bioadhesives on fresh porcine skin ($n = 3$). (I) Average adhesion strength of G-H4-P4 bioadhesives on dry or wet fresh porcine skin ($n = 3$). (J–M) Lap-shear adhesion strength as a function of washing time with water (J) or NS (L) after adhesion to porcine skin, and representative lap-shear adhesion curves for rinsing with water (K) or NS (M). (N) and (O) Average lap-shear adhesion strength of the G-H4-P4 and G-P bioadhesives on porcine skin at different temperatures, respectively. (P) and (Q) T-peeling curves of G-H4-P4 and G-P bioadhesives on porcine skin at different temperatures, respectively.

weight ratios between 2 and 4 were selected for subsequent investigations.

3.2. Mechanical properties, injectability, and adhesive capabilities of the CPTG bioadhesives

The CPTG bioadhesives exhibited liquid-like behavior, as evidenced by the loss modulus (G'') being close to or even slightly higher than the

storage modulus (G'), which was crucial for the development of size-adaptable bioadhesives (Fig. 2B and Video S4). The bioadhesive with the highest PA content (G-H4-P4) demonstrated the highest storage modulus when the HU content was kept constant (Fig. 2C). Furthermore, the mechanical strength of the developed CPTG bioadhesive without HU was much higher than that of the bioadhesives containing HU, indicating that HU adversely affected the strength of the bioadhesives (Figs. S3F–S3G). When they were immersed in an aqueous environment, the storage modulus of the fabricated CPTG bioadhesives increased by nearly an order of magnitude due to the diffusion-triggered structural densification (Fig. 2D and E). Accordingly, the color of the bioadhesives changed immediately (Fig. S3A and Video S1), and the pore size decreased (Fig. S3B), as HU diffused much faster than PA (Fig. 2D). This rapid diffusion released hydrogen-bonding interaction sites on gelatin, enhancing the interaction between PA and gelatin.

Supplementary data related to this article can be found online at <https://doi.org/10.1016/j.bioactmat.2024.12.014>

It is worth noting that with increasing oscillation frequencies, both the storage modulus (G') and loss modulus (G'') of the developed CPTG bioadhesives increased, indicating dynamic crosslinking [12] (Fig. 2B). The bioadhesives (G-H4-Py) composed of a dynamic crosslinking network also demonstrated good self-healing properties (Fig. S3C). Increasing the shear rate reduced the viscosity of both bioadhesives (Fig. 2F). However, due to the uncontrollable phase transition of the traditional gelatin-based bioadhesives at low temperatures, the viscosity of G-P was too high (1100.00 Pa·s) for injection at 4 °C. In contrast, the viscosity of the G-H4-P4 bioadhesive was 8.56 Pa·s under the same conditions, which was suitable for injection [49].

The CPTG bioadhesives demonstrated efficient adhesion to fresh porcine skin within 10 s, achieving a maximum adhesion strength of 30.92 ± 1.95 kPa (Fig. 2H). The porcine samples adhered with the GPTC bioadhesive, which had an adhesion area of 0.62 cm², were able to support a minimum weight of 200 g, as confirmed in Video S2 (Supporting Information). This bioadhesive adhered tightly to the porcine skin without detachment after bending, twisting, and stretching (Fig. 2G). As expected, the diffusion-triggered transition enhanced the adhesion strength [45]. The GPTC bioadhesive (G-H4-P4) showed higher adhesion strength to wet porcine skin compared to dry porcine skin (Fig. 2I). Furthermore, the adhesion strength increased significantly after rinsing the adhesive samples with distilled water or NS (Fig. 2J–M). The maximum adhesion strength reached 151.63 ± 10.79 and 192.69 ± 6.81 kPa after rinsing with water or saline, respectively. These findings indicated the GPTC bioadhesive possessed the capability of self-enhanced interfacial adhesion upon contact with moist wound tissues. As such, the CPTG bioadhesive (G-H4-P4) maintained high adhesion energy at lower temperatures compared to the conventional gelatin-based bioadhesive (G-P). The adhesion energies of G-H4-P4 were 52.6, 51.3, and 47.8 J m⁻² at 37, 25, and 4 °C, respectively (Fig. 2P). The adhesion energies of G-P were 132.8, 32.0, and 8.2 J m⁻² at 37, 25, and 4 °C, respectively, indicating significant differences (Fig. 2Q). Likewise, the G-P bioadhesive presented notable variations in the shear adhesion strengths across different temperatures (Fig. 2O). In contrast, the shear adhesion strengths of the G-H4-P4 bioadhesive remained consistent regardless of temperature fluctuations (Fig. 2N). These findings demonstrated that the CPTG bioadhesive (G-H4-P4) maintained stable adhesion properties across a range of temperatures. Besides, the CPTG bioadhesives exhibited universal adhesion to various tissues, including the stomach, colon, and liver (Figs. S3H, S3E, and S3I). Furthermore, this bioadhesive could also effectively seal leakage in the porcine stomach (Fig. 2G).

Supplementary data related to this article can be found online at <https://doi.org/10.1016/j.bioactmat.2024.12.014>

3.3. Degradability, biocompatibility and biological activities of the CPTG bioadhesives

The CPTG bioadhesives presented superior biodegradability, with their dry weight decreasing to ~20% within 5 days (Fig. S4A). Likewise, they exhibited favorable biocompatibility and hemocompatibility (Fig. S4B, S4C and S4D). These findings suggest that the CPTG bioadhesive is a promising candidate for use as an effective wound dressing. To investigate the biological activities of the CPTG bioadhesives, we induced RAW 264.7 macrophage cells with lipopolysaccharide (LPS) [50,51] to mimic the imbalanced microenvironment of diabetes. We then analyzed gene expression in RAW 264.7 cells treated with the CPTG bioadhesives using RNA-seq (Fig. 3A). The hierarchical cluster analysis revealed that the expression of pro-inflammatory M1 phenotype-related genes (CCL2, CCL3, CCL4, CCL5, CXCL10, CXCL2, IL-6, TNF, NOS2, PTGS2, and IL-1 β) decreased in the experimental group treated with the bioadhesives (Fig. 3B). At the same time, the expression of anti-inflammatory M2 phenotype-related genes (S100A4 and CXCR4) and angiogenesis-related genes (Ang) increased following treatment with the bioadhesives. The Gene ontology (GO) analysis demonstrated that these genes were primarily enriched in biological processes related to wound healing, immune response, bacterial defense, and response to oxidative stress (Fig. 3C). Further, the Kyoto Encyclopedia of Genes and Genomes (KEGG) pathway classification analysis indicated enrichment of differentially expressed genes associated with immune and diabetes pathways, such as cytokine-cytokine receptor interaction, JAK-STAT signalling pathway, and AGE-RAGE signaling pathway (Fig. 3D).

Subsequently, we demonstrated that the CPTG bioadhesives exhibited efficient anti-Gram-positive bacterial activity, as confirmed by our *in vitro* experiments (Fig. S5A). The number of bacteria in the experimental groups was significantly lower than in the control group, showing a 56.0% decrease in *E. coli* colonies, while the killing ratio against *S. aureus* was 97.6% (Fig. S5B). Likewise, each bioadhesive exhibited excellent ROS scavenging performance, with DPPH scavenging reaching nearly 80% (Fig. S5C). Compared to the ROS-up mediated positive control group, significant fluorescence quenching was observed in the bioadhesive-treated group, with fluorescence intensity comparable to that of the negative control group (Fig. 4A). Similar results were observed in the L929 fibroblast cells (Fig. S5D).

3.4. Modulation of the immune microenvironment by the CPTG bioadhesives

The CPTG bioadhesives demonstrated a significant capability to regulate the immune microenvironment. RAW 264.7 cells incubated with LPS exhibited notable deformation compared to those treated with PBS (blank group), showing expanded lamellar cellular structures and elongated filopodia. Notably, the addition of the bioadhesive extract caused the filopodia to retract, resulting in cells becoming more spherical with a considerable reduction in area (Fig. 4B). Our quantitative analysis revealed that the average cell area expanded 5.89-fold for LPS-treated cells and 2.88-fold for cells treated with both LPS and G-H4-P4, compared to the blank group (Fig. 4C), which aligns with the characteristics of M1 and M2 phenotypes [52]. Fluorescence-activated cell sorter (FACS) analysis indicated that the LPS-treated cells had the highest density of inducible nitric oxide synthase (iNOS⁺) cells (M1 phenotype), while the addition of the bioadhesive extract significantly induced macrophage mannose receptor (CD206⁺) cells (M2 phenotype), suggesting that the G-H4-P4 bioadhesive can modulate macrophage phenotype transformation (Fig. 4D and E, and S5E).

Immunofluorescence staining indicated that the group treated with LPS resulted in the most intense iNOS staining, implying a pronounced proinflammatory response, whereas the group cotreated with LPS and G-H4-P4 displayed weaker fluorescence intensity (Fig. 4J). Meantime, the group cotreated with LPS and G-H4-P4 showed a significant increase in CD206 staining compared to other groups. Real-time quantitative PCR

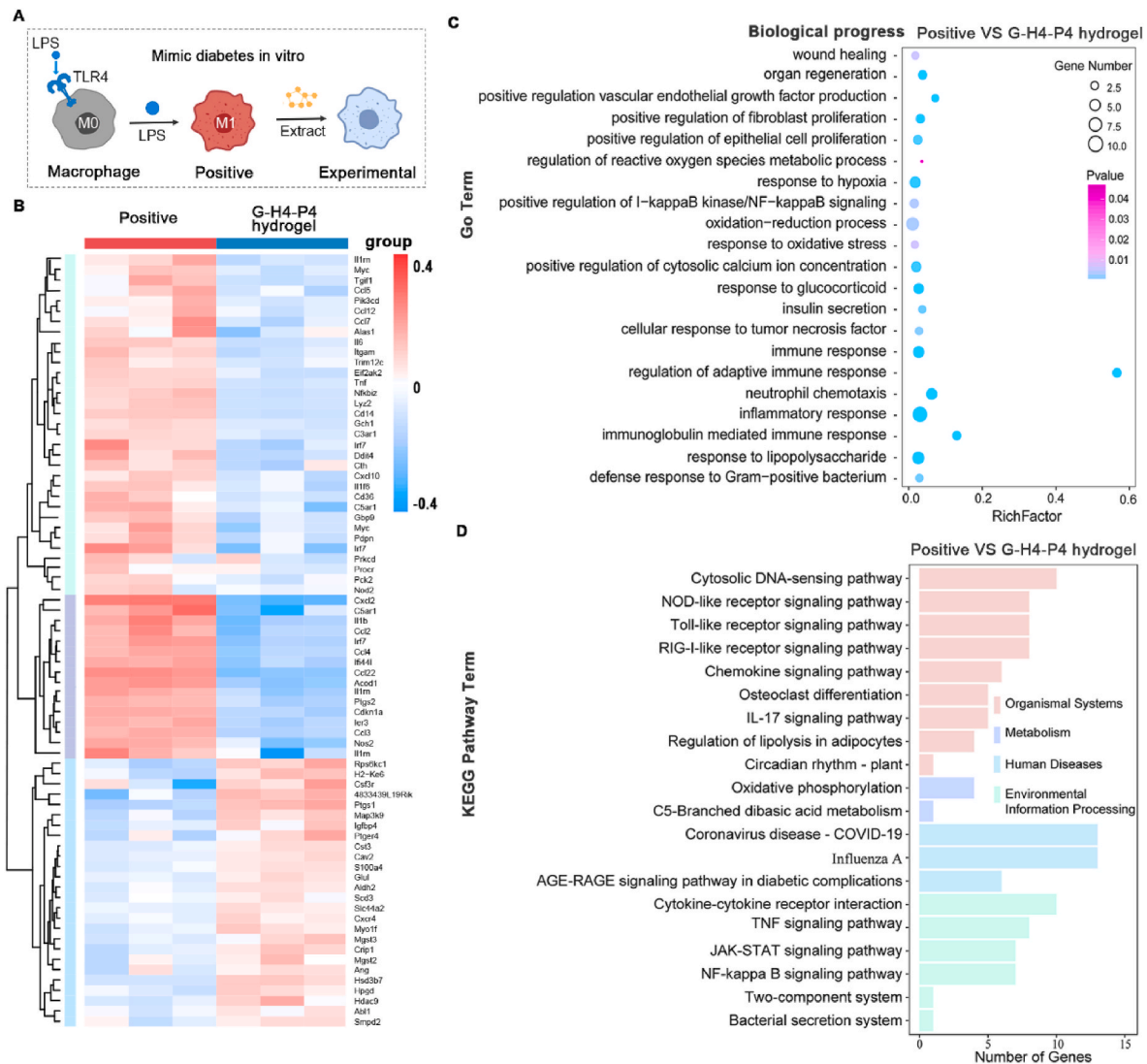


Fig. 3. Gene expression and functional enrichment analysis.

(A) Schematic representation of diabetes mimicking in RAW264.7 cells and subsequent treatment with the G-H4-P4 bioadhesive. (B) Heat map showing upregulated and downregulated genes in LPS-treated RAW264.7 cells after treatment with the G-H4-P4 bioadhesive. (C) Gene ontology (GO) enrichment analysis of biological processes. (D) KEGG pathway enrichment analysis for the G-H4-P4 bioadhesive.

(RT-qPCR) further revealed that the expression levels of the M1-related genes (e.g., IL-1 β and iNOS) were elevated in the LPS group but decreased after they were treated with the G-H4-P4 bioadhesive. Conversely, the expression levels of the M2-related genes (e.g., Arg-1 and CD206) were upregulated in cells treated with the G-H4-P4 bioadhesive extract (Fig. 4F–I). Consequently, the developed CPTG bioadhesives are well-suited for wound closure due to their immune microenvironment regulation properties.

3.5. Diabetic wound healing assays based on the CPTG bioadhesives

The developed CPTG bioadhesives were evaluated for their effectiveness in diabetic wound healing assays (YSY-DWLL-2021031). Specifically, the G-H4-P4 bioadhesive was applied to full-thickness wounds on diabetic mice using a syringe (Fig. 5A). For comparison, the commercial Tegaderm film was employed to treat the diabetic mouse wounds. Additionally, untreated full-thickness wounds were included as a control group in the diabetic wound healing assays. Our experimental results demonstrated that the G-H4-P4 bioadhesive adhered firmly to the wound within just 10 s of gentle pressing, facilitating subsequent applications (Video S3). Compared to the commercial group, the

bioadhesive remained firmly adhered to the wound even after 3 days. Furthermore, the bioadhesive had the fastest healing efficiency, with nearly complete healing observed by the 14th day (Fig. 5B). On the third day, the bioadhesive-treated group exhibited 59.4% wound closure, outperforming both the control group (39.1%) and the commercial group (45.5%). On the 14th day, the wound area in the untreated control group remained at 15.86%, while that in the commercial group was 13.53%. In contrast, the G-H4-P4 bioadhesive group reduced the wound area to 6.86% (Fig. 5C). Besides, the untreated control group showed a pronounced inflammatory response characterized by severe neutrophils infiltration, while the groups using the Tegaderm film and G-H4-P4 bioadhesive demonstrated only a mild inflammatory response (Figs. S7A and S7B). In comparison with the untreated and commercial groups, the bioadhesive-treated group exhibited a significant decrease in the M1 macrophages (F4/80⁺, iNOS⁺) but a simultaneous increase in the M2 macrophages (F4/80⁺, CD163⁺) (Fig. 5D). These findings suggested that the bioadhesive possessed the capacity to regulate macrophage polarization *in vivo*. Furthermore, the immunohistochemical staining of cytokines, including IL-1 β , TNF- α , Arg-1 and IL-10, confirmed the ability of the G-H4-P4 bioadhesive to modulate the immune microenvironment. The G-H4-P4 bioadhesive group exhibited the lowest expression levels

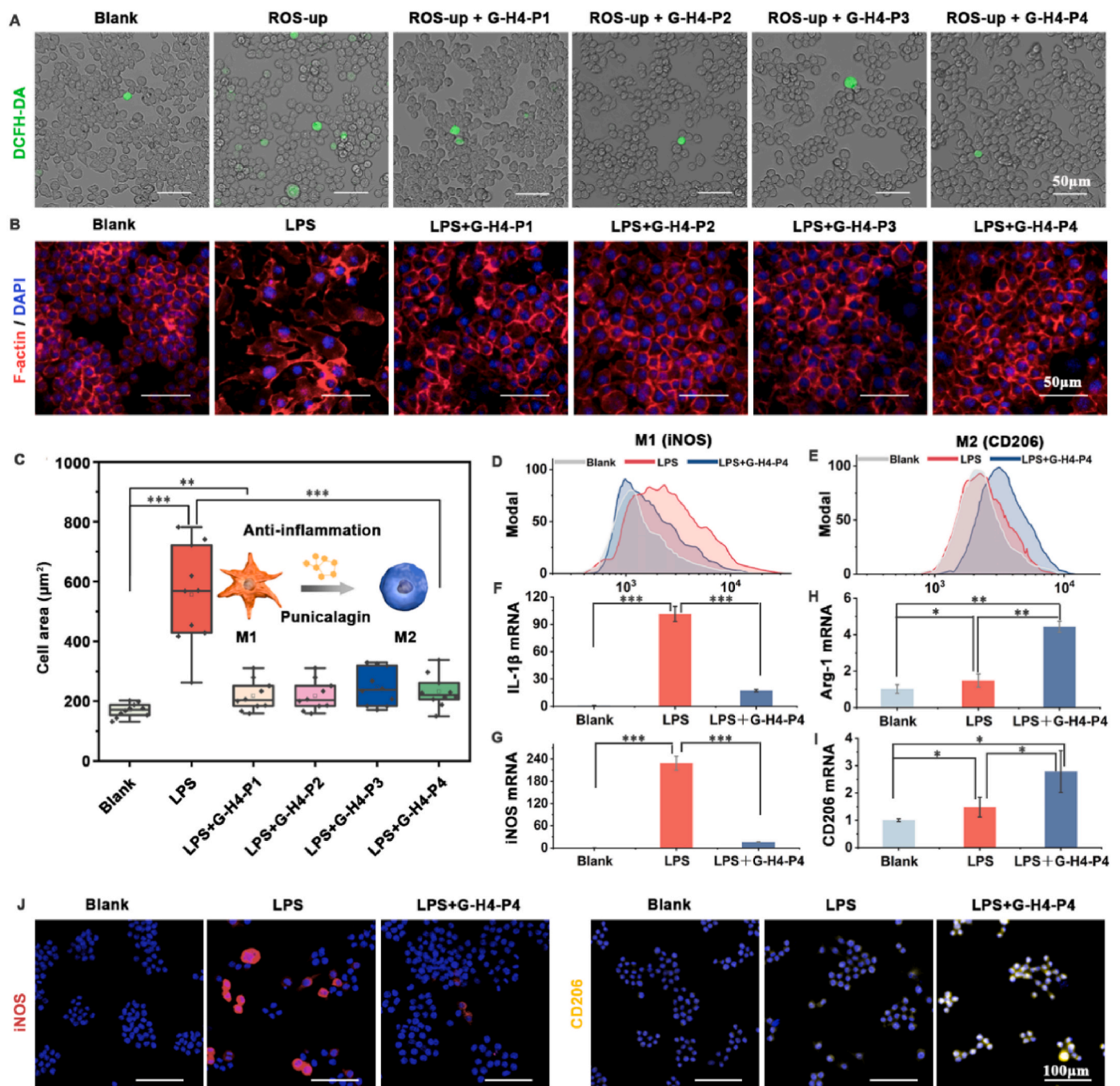


Fig. 4. *In vitro* immune microenvironment regulation of the G-H4-P4 bioadhesive. (A) DCFH-DA fluorescence staining on RAW264.7 macrophages to assess the anti-oxidative capability of the G-H4-Py bioadhesives ($y = 1, 2, 3, 4$). (B) F-actin staining to observe membrane morphological alterations in RAW 264.7 cells. Phalloidin (red) stains F-actin, and DAPI (blue) stains nuclei. (C) Quantitative analysis of cell areas. Data are expressed as Mean \pm SD ($n = 10$). (D) and (E) Fluorescence-activated cell sorter (FACS) analysis of protein expression levels of M1 (iNOS) and M2 (CD206), respectively, after 48 h of treatment ($n = 3$). (F) and (I) Real-time quantitative PCR analysis of gene expression levels of M1 (IL-1 β , iNOS) and M2 (Arg-1, CD206), respectively, after 24 h of treatment ($n = 3$). (J) Fluorescence images of RAW 264.7 cell phenotypes after different treatments. Blue, red, and yellow colors represent DAPI, iNOS, and CD206, respectively. * $p < 0.05$, ** $p < 0.01$, *** $p < 0.001$.

of IL-1 β and TNF- α (pro-inflammatory cytokines) as shown in Fig. 6A–C. Additionally, the signals for Arg-1 and IL-10 (Anti-inflammatory cytokines) in the G-H4-P4 bioadhesive group were much stronger than the untreated control and Tegaderm groups (Fig. 6D and E). These results illustrated the ability of the G-H4-P4 bioadhesive to effectively modulate the immune microenvironment.

Supplementary data related to this article can be found online at <https://doi.org/10.1016/j.bioactmat.2024.12.014>

Moreover, we observed that rinsing the bioadhesive covering the

wound with normal saline (NS) enhanced the expression of α SMA (Fig. 5E), a marker indicative of fibroblast to myofibroblast conversion. The percentage of α SMA⁺ cells in the G-H4-P4 bioadhesive-treated group (26.7%) was higher than that in the untreated control group (20.8%), with the NS-rinsed G-H4-P4 group showing the highest percentage (37.69%) (Fig. 5F). We hypothesize that the diffusion of HU accelerated the adhesion process, thereby creating contractile stress on the wound and activating a greater number of α SMA⁺ cells. Our histological staining revealed that, compared to other groups, the

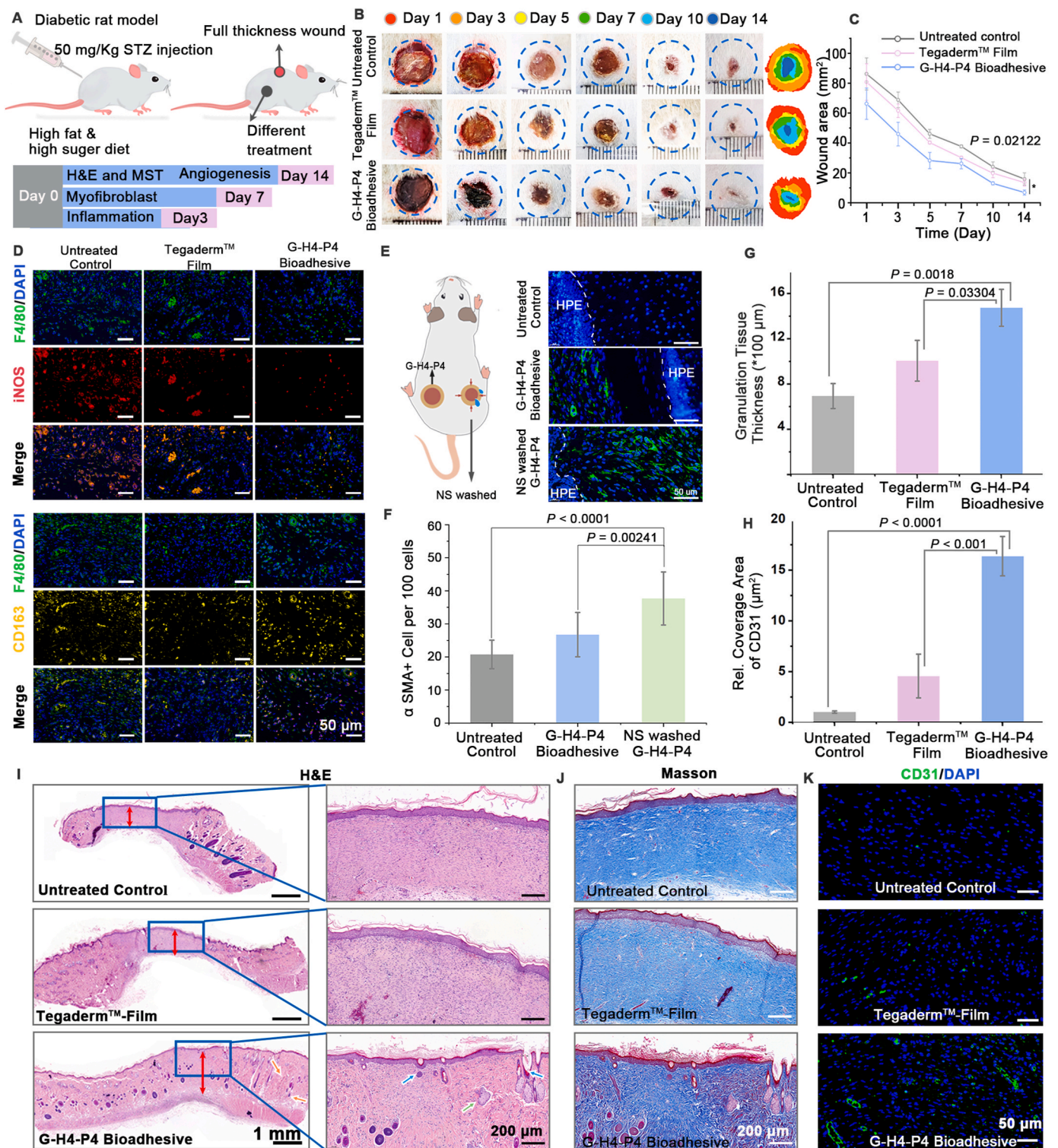


Fig. 5. *In vivo* diabetic wound healing assays. (A) Schematic representation of the establishment of the diabetic chronic wound rat model and the operational timeline. (B) The G-H4-P4 bioadhesive promoted diabetic wound repair and regeneration *in vivo*, demonstrating the progression of wound closure on days 1, 3, 5, 7, 10, and 14. (C) Quantitative analysis of wound area for each group, with p-values indicating comparisons between the untreated control and the G-H4-P4 group. (D) Immunofluorescence images of macrophages in wound tissues on day 3, stained with F4/80 (green), iNOS (red), and CD163 (yellow). Nuclei were stained with DAPI (blue). (E) Representative immunofluorescence images for the αSMA cells on day 7, where the illustration showed wound contraction after washing with normal saline (NS). HPE was the abbreviation of hyperproliferative epidermis. (F) Statistical results of αSMA⁺ cells per 100 cells based on the immunofluorescence images as presented in (E). (G) Statistical results of granulation tissue thickness. (H) Statistical results of the area of CD31. (I) H&E staining of the wound area on day 14. (J) Masson staining of the wound area on day 14. (K) CD31 staining of angiogenesis in the wound area on day 14. Data are presented as Mean ± SD (n = 3).

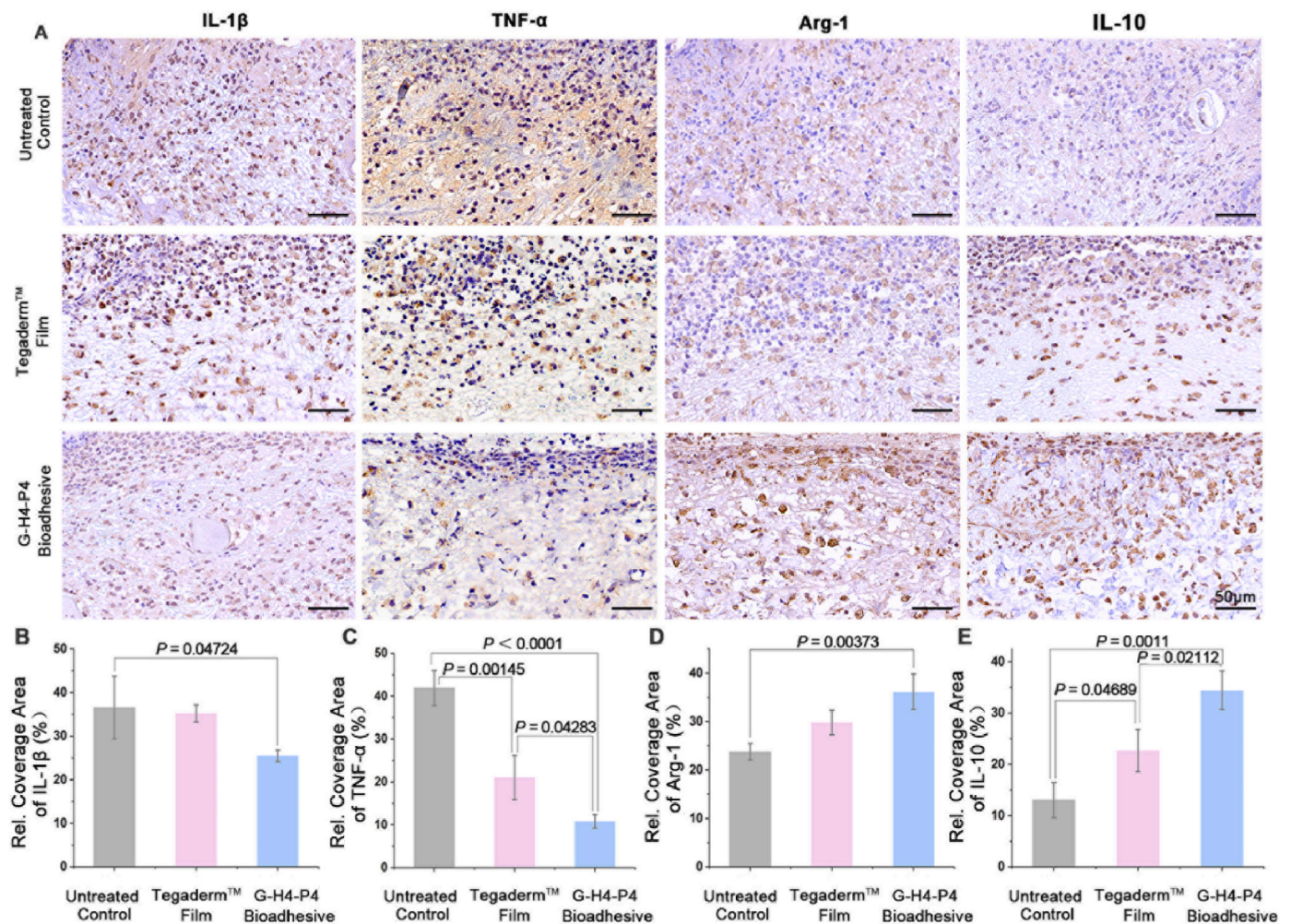


Fig. 6. *In vivo* immunological assays of cytokine levels. (A) Representative immunohistochemistry pictures for IL-1 β , TNF- TNF- α , Arg-1 and IL-10 on day 3. (B) Statistical results of the area of IL-1 β , TNF- TNF- α , Arg-1 and IL-10. Data are presented as Mean \pm SD (n = 3).

bioadhesive-treated group formed mature epithelial structures, including hair follicles (blue arrows), squamous epithelium (green arrows), sebaceous glands, and ducts of sweat glands (orange arrows) (Fig. 5I). Additionally, the thickness of granulation tissue (red arrows) was significantly increased in the bioadhesive group. Specifically, the thickness of granulation tissue in the G-H4-P4 bioadhesive group was 2.1- and 1.4-fold higher than in the untreated and commercial groups, respectively (Fig. 5G). Also, the bioadhesive group had the highest collagen deposition (Fig. 5J), consistent with visual observations in the digital photographs. The concentrations of blood glucose levels were higher than 16.7 mmol L⁻¹ during the animal experiments (Fig. S6).

Finally, angiogenesis in the chronic wound healing was assessed using the CD31 antibody, which was highly expressed by endothelial cells and also known as platelet endothelial cell adhesion molecule (PECAM-1) [50]. It was found that the commercial Tegaderm film-treated group led to a partial enhancement in the area of CD31⁺ cells, but this effect was inferior to that of the bioadhesive-treated group (Fig. 5K). The area of CD31⁺ cells in the bioadhesive-treated group was 15.7- and 3.4-fold higher than in the untreated and commercial Tegaderm film-treated groups, respectively (Fig. 5H). These results indicated that treatment with the G-H4-P4 bioadhesive could effectively promote angiogenesis. In summary, the developed CPTG bioadhesive demonstrated superior performance compared to the commercial wound dressings due to its stable adhesion and ability to regulate the immune microenvironment, making it a promising biomaterial for biomedical engineering applications.

4. Conclusion and perspectives

Owing to the excellent biocompatibility and biodegradability, gelatin-based biomaterials have been widely applied in various engineering fields like biomedicine, biomanufacturing, soft robotics, tissue engineering and wearable and implantable electronics. In this work, we developed CPTG bioadhesives primarily composed of gelatin, HU and PA, which enabled a controllable phase transition. As a result, these bioadhesives exhibited adjustable mechanical properties, excellent injectability, and stable adhesion to biological tissues even at 4 °C. As the HU molecules diffused out of the bioadhesives at the adhesive interfaces, they achieved self-reinforcing interfacial adhesion upon contact with the moist wound tissues. More importantly, we reported that the designed bioadhesives had the capability to regulate the immune microenvironment due to the introduction of PA. Using a diabetic chronic wound rat model, we demonstrated that these bioadhesives could significantly accelerate diabetic wound healing, which presents an alternative therapeutic strategy for the clinical management of chronic diabetic wounds through immune regulation. Also, this work provides new insights into the design of controllable phase-transition gelatin-based biomaterials, which are expected to have important applications in various engineering fields.

There remains significant potential for exploration regarding the clinical applications of this bioadhesive. Diabetic foot ulcers (DFUs) represent a severe complication of diabetes and are the leading cause of non-traumatic lower limb amputations [53], posing substantial threats

to patient health [54]. The standard clinical management process for DFUs typically extends over a duration of 12 weeks or longer [20,55]. However, the GPTC bioadhesive demonstrated a rapid degradation rate within five days. It is essential to adjust the degradation rates according to different wound types and clinical scenarios. It is well-known that polyvinyl alcohol (PVA) is an FDA-approved biocompatible synthetic polymer that can interact with the pyrogallol structure [56] and exhibits a notably slow degradation rate [57,58]. Thus, it is possible that the introduction of PVA may contribute to an extension of the degradation time of the CPTG bioadhesives. Although the GPTC bioadhesive provides acceleration of diabetic wound healing in rat models, the developed GPTC bioadhesive requires further validation in large animal models. Furthermore, the GPTC bioadhesives are synthesized using a two-step method, which is inherently suitable for large-scale production. The formulation of the developed adhesive includes several materials with good biocompatibility. Gelatin is recognized as an FDA-approved pharmaceutical excipient, while the natural PA and HU are widely utilized as raw materials in moisturizing and skincare products. Although the development of GPTC bioadhesives is still in its early stages, it presents a promising candidate for diabetic wound healing materials.

CRedit authorship contribution statement

Zhuoling Tian: Conceptualization, Investigation, Methodology, Formal analysis, Data curation, Writing – original draft. **Ruoheng Gu:** Investigation, Methodology, Software. **Wenyue Xie:** Investigation, Methodology, Formal analysis. **Xing Su:** Investigation, Funding acquisition. **Zuoying Yuan:** Methodology, Formal analysis. **Zhuo Wan:** Methodology, Formal analysis. **Hao Wang:** Investigation, Formal analysis, Funding acquisition. **Yaqian Liu:** Methodology, Formal analysis. **Yuting Feng:** Methodology, Formal analysis. **Xiaozhi Liu:** Methodology, Formal analysis, Funding acquisition. **Jianyong Huang:** Conceptualization, Investigation, Methodology, Project administration, Formal analysis, Funding acquisition, Writing – review & editing.

Ethics approval and consent to participate

The animal protocols were approved by the Animal Ethics Committee of Yi Shengyuan Genome Technology (Tianjin) Co., Ltd. (protocol number YSY-DWLL-2021031).

Declaration of competing interest

The authors declare that they have no known competing financial interests or personal relationships that could have appeared to influence the work reported in this paper.

Acknowledgements

This work was supported by National Key Research and Development Program of China (grant nos. 2021YFA1000200 and 2021YFA1000201), National Natural Science Foundation of China (grant nos. 12372175, 12102010 and 52363019), Tianjin Municipal Science and Technology Plan Project (grant no. 24ZYCGSY00650), and Tianjin Health Technology Project (grant no. TJWJ2022XK043).

Appendix A. Supplementary data

Supplementary data to this article can be found online at <https://doi.org/10.1016/j.bioactmat.2024.12.014>.

References

- [1] J. Alipal, N.A.S. Mohd Pu'ad, T.C. Lee, N.H.M. Nayan, N. Sahari, H. Basri, M. I. Idris, H.Z. Abdullah, A review of gelatin: properties, sources, process,

- applications, and commercialisation, *Mater. Today: Proc.* 42 (2021) 240–250, <https://doi.org/10.1016/j.matpr.2020.12.922>.
- [2] C.H. Barty-King, C.L.C. Chan, R.M. Parker, M.M. Bay, R. Vadrucci, M. De Volder, S. Vignolini, Mechanochromic, structurally colored, and edible hydrogels prepared from hydroxypropyl cellulose and gelatin, *Adv. Mater.* 33 (2021) 2102112, <https://doi.org/10.1002/adma.202102112>.
- [3] C.H. Yang, Z.G. Suo, Hydrogel ionotronics, *Nat. Rev. Mater.* 3 (2018) 125–142, <https://doi.org/10.1038/s41578-018-0018-7>.
- [4] C.-G. Han, X. Qian, Q. Li, B. Deng, Y. Zhu, Z. Han, W. Zhang, W. Wang, S.-P. Feng, G. Chen, W. Liu, Giant thermopower of ionic gelatin near room temperature, *Science* 368 (2020) 1091–1098, <https://doi.org/10.1126/science.aaz5045>.
- [5] S. Sharifi, M.M. Islam, H. Sharifi, R. Islam, D. Koza, F. Reyes-Ortega, D. Alba-Molina, P.H. Nilsson, C.H. Dohlman, T.E. Mollnes, et al., Tuning gelatin-based hydrogel towards bioadhesive ocular tissue engineering applications, *Bioact. Mater.* 6 (2021) 3947–3961, <https://doi.org/10.1016/j.bioactmat.2021.03.042>.
- [6] A. Maihemuti, H. Zhang, X. Lin, Y. Wang, Z. Xu, D. Zhang, Q. Jiang, 3D-printed fish gelatin scaffolds for cartilage tissue engineering, *Bioact. Mater.* 26 (2023) 77–87, <https://doi.org/10.1016/j.bioactmat.2023.02.007>.
- [7] H. Yuk, C.E. Varela, C.S. Nabzdyk, X. Mao, R.F. Padera, E.T. Roche, X. Zhao, Dry double-sided tape for adhesion of wet tissues and devices, *Nature* 575 (2019) 169–174, <https://doi.org/10.1038/s41586-019-1710-5>.
- [8] X. Qi, Y. Xiang, E. Cai, X. Ge, X. Chen, W. Zhang, Z. Li, J. Shen, Inorganic–organic hybrid nanomaterials for photothermal antibacterial therapy, *Coord. Chem. Rev.* 496 (2023) 215426, <https://doi.org/10.1016/j.ccr.2023.215426>.
- [9] G. Li, F. Gao, D. Yang, L. Lin, W. Yu, J. Tang, R. Yang, M. Jin, Y. Gu, P. Wang, E. Lu, ECM-mimicking composite hydrogel for accelerated vascularized bone regeneration, *Bioact. Mater.* 42 (2024) 241–256, <https://doi.org/10.1016/j.bioactmat.2024.08.035>.
- [10] Y. Liu, L.M. Geever, J.E. Kennedy, C.L. Higginbotham, P.A. Cahill, G. B. McGuinness, Thermal behavior and mechanical properties of physically crosslinked PVA/Gelatin hydrogels, *J. Mech. Behav. Biomed. Mater.* 3 (2010) 203–209, <https://doi.org/10.1016/j.jmbbm.2009.07.001>.
- [11] L. Xu, C. Wang, Y. Cui, A. Li, Y. Qiao, D. Qiu, Conjoined-network rendered stiff and tough hydrogels from biogenic molecules, *Sci. Adv.* 5 (2019) eaau3442, <https://doi.org/10.1126/sciadv.aau3442>.
- [12] L. Zhou, C. Dai, L. Fan, Y. Jiang, C. Liu, Z. Zhou, P. Guan, Y. Tian, J. Xing, X. Li, et al., Injectable self-healing natural biopolymer-based hydrogel adhesive with thermoresponsive reversible adhesion for minimally invasive surgery, *Adv. Funct. Mater.* 31 (2021) 2007457, <https://doi.org/10.1002/adfm.202007457>, 2007457.
- [13] M.D. Shoulders, R.T. Raines, Collagen structure and stability, *Annu. Rev. Biochem.* 78 (2009) 929–958, <https://doi.org/10.1146/annurev.biochem.77.032207.120833>.
- [14] A.I. Van den Bulcke, B. Bogdanov, N. De Rooze, E.H. Schacht, M. Cornelissen, H. Berghmans, Structural and rheological properties of methacrylamide modified gelatin hydrogels, *Biomacromolecules* 1 (2000) 31–38, <https://doi.org/10.1021/bm990017d>.
- [15] A. Todd, Rigidity factor of gelatin gels, *Nature* 191 (1961) 567–569, <https://doi.org/10.1038/191567a0>.
- [16] L. Lan, J. Ping, H. Li, C. Wang, G. Li, J. Song, Y. Ying, Skin-Inspired all-natural biogel for bioadhesive interface, *Adv. Mater.* 36 (2024) 2401151, <https://doi.org/10.1002/adma.202401151>.
- [17] A.I. Sarabia, M.C. Gomez-Guillen, P. Montero, The effect of added salts on the viscoelastic properties of fish skin gelatin, *Food Chem.* 70 (2000) 71–76, [https://doi.org/10.1016/s0308-8146\(00\)00073-x](https://doi.org/10.1016/s0308-8146(00)00073-x).
- [18] H. Ravanbakhsh, Z. Luo, X. Zhang, S. Maharjan, H.S. Mirkarimi, G. Tang, C. Chávez-Madero, L. Mongeau, Y.S. Zhang, Freeform cell-laden cryobioprinting for shelf-ready tissue fabrication and storage, *Matter* 5 (2022) 573–593, <https://doi.org/10.1016/j.matt.2021.11.020>.
- [19] H. Xia, Z. Dong, Q. Tang, R. Ding, Y. Bai, K. Zhou, L. Wu, L. Hao, Y. He, J. Yang, et al., Glycopeptide-based multifunctional hydrogels promote diabetic wound healing through pH regulation of microenvironment, *Adv. Funct. Mater.* 33 (2023) 2215116, <https://doi.org/10.1002/adfm.202215116>.
- [20] V. Falanga, Wound healing and its impairment in the diabetic foot, *Lancet* 366 (2005) 1736–1743, [https://doi.org/10.1016/S0140-6736\(05\)67700-8](https://doi.org/10.1016/S0140-6736(05)67700-8).
- [21] T.M. Raimondo, D.J. Mooney, Functional muscle recovery with nanoparticle-directed M2 macrophage polarization in mice, in: Proceedings of the National Academy of Sciences, vol. 115, 2018, pp. 10648–10653, <https://doi.org/10.1073/pnas.1806908115>.
- [22] F. Shu, H. Huang, S. Xiao, Z. Xia, Y. Zheng, Netrin-1 co-cross-linked hydrogel accelerates diabetic wound healing in situ by modulating macrophage heterogeneity and promoting angiogenesis, *Bioact. Mater.* 39 (2024) 302–316, <https://doi.org/10.1016/j.bioactmat.2024.04.019>.
- [23] X. Qi, E. Cai, Y. Xiang, C. Zhang, X. Ge, J. Wang, Y. Lan, H. Xu, R. Hu, J. Shen, An immunomodulatory hydrogel by hyperthermia-assisted self-cascade glucose depletion and ROS scavenging for diabetic foot ulcer wound therapeutics, *Adv. Mater.* 35 (2023) 2306632, <https://doi.org/10.1002/adma.202306632>.
- [24] S. Shang, K. Zhuang, J. Chen, M. Zhang, S. Jiang, W. Li, A bioactive composite hydrogel dressing that promotes healing of both acute and chronic diabetic skin wounds, *Bioact. Mater.* 34 (2024) 298–310, <https://doi.org/10.1016/j.bioactmat.2023.12.026>.
- [25] S. Zhu, B. Zhao, M. Li, H. Wang, J. Zhu, Q. Li, H. Gao, Q. Feng, X. Cao, Microenvironment responsive nanocomposite hydrogel with NIR photothermal therapy, vascularization and anti-inflammation for diabetic infected wound healing, *Bioact. Mater.* 26 (2023) 306–320, <https://doi.org/10.1016/j.bioactmat.2023.03.005>.

- [26] X. Qi, X. Ge, X. Chen, E. Cai, Y. Xiang, H. Xu, Y. Li, Y. Lan, Y. Shi, H. Deng, J. Shen, An immunoregulation hydrogel with controlled hyperthermia-augmented oxygenation and ROS scavenging for treating diabetic foot ulcers, *Adv. Funct. Mater.* 34 (2024) 2400489, <https://doi.org/10.1002/adfm.202400489>.
- [27] X. Qi, Y. Shi, C. Zhang, E. Cai, X. Ge, Y. Xiang, Y. Li, B. Zeng, J. Shen, A hybrid hydrogel with intrinsic immunomodulatory functionality for treating multidrug-resistant *Pseudomonas aeruginosa* infected diabetic foot ulcers, *ACS Mater. Lett.* 6 (2024) 2533–2547, <https://doi.org/10.1021/acsmaterialslett.4c00392>.
- [28] Y. Hou, Y. Li, Y. Li, D. Li, T. Guo, X. Deng, H. Zhang, C. Xie, X. Lu, Tuning water-resistant networks in mussel-inspired hydrogels for robust wet tissue and bioelectronic adhesion, *ACS Nano* 17 (2023) 2745–2760, <https://doi.org/10.1021/acsnano.2c11053>.
- [29] S.M. Toshi, A.G. Marangoni, Determination of the maximum gelation temperature in gelatin gels, *Appl. Phys. Lett.* 84 (2004) 4242–4244, <https://doi.org/10.1063/1.1756210>.
- [30] J. Bella, B. Brodsky, H.M. Berman, Hydration structure of a collagen peptide, *Structure* 3 (1995) 893–906, [https://doi.org/10.1016/S0969-2126\(01\)00224-6](https://doi.org/10.1016/S0969-2126(01)00224-6).
- [31] S. Jo, T. Kim, V.G. Iyer, W. Im, CHARMM-GUI: a web-based graphical user interface for CHARMM, *J. Comput. Chem.* 29 (2008) 1859–1865, <https://doi.org/10.1002/jcc.20945>.
- [32] J. Huang, S. Rauscher, G. Nawrocki, T. Ran, M. Feig, B.L. de Groot, H. Grubmüller, A.D. MacKerell, CHARMM36m: an improved force field for folded and intrinsically disordered proteins, *Nat. Methods* 14 (2017) 71–73, <https://doi.org/10.1038/nmeth.4067>.
- [33] W.M. Brown, A. Kohlmeyer, S.J. Plimpton, A.N. Tharrington, Implementing molecular dynamics on hybrid high performance computers – particle–particle particle-mesh, *Comput. Phys. Commun.* 183 (2012) 449–459, <https://doi.org/10.1016/j.cpc.2011.10.012>.
- [34] W.L. Jorgensen, J. Chandrasekhar, J.D. Madura, R.W. Impey, M.L. Klein, Comparison of simple potential functions for simulating liquid water, *J. Chem. Phys.* 79 (1983) 926–935, <https://doi.org/10.1063/1.445869>.
- [35] W. Humphrey, A. Dalke, K. Schulten, VMD: visual molecular dynamics, *J. Mol. Graph. Model.* 14 (1996) 33–38, [https://doi.org/10.1016/0263-7855\(96\)00018-5](https://doi.org/10.1016/0263-7855(96)00018-5).
- [36] A. Luzar, D. Chandler, Effect of environment on hydrogen bond dynamics in liquid water, *Phys. Rev. Lett.* 76 (1996) 928–931, <https://doi.org/10.1103/PhysRevLett.76.928>.
- [37] Y. Liu, P. Wang, X. Su, L. Xu, Z. Tian, H. Wang, G. Ji, J. Huang, Electrically programmable interfacial adhesion for ultrastrong hydrogel bonding, *Adv. Mater.* 34 (2022) 2108820, <https://doi.org/10.1002/adma.202108820>.
- [38] N.G. Voron'ko, S.R. Derkach, M.A. Vovk, P.M. Tolstoy, Complexation of κ-carrageenan with gelatin in the aqueous phase analysed by 1H NMR kinetics and relaxation, *Carbohydr. Polym.* 169 (2017) 117–126, <https://doi.org/10.1016/j.carbpol.2017.04.010>.
- [39] X. Su, Y. Luo, Z. Tian, Z. Yuan, Y. Han, R. Dong, L. Xu, Y. Feng, X. Liu, J. Huang, Ctenophore-inspired hydrogels for efficient and repeatable underwater specific adhesion to biotic surfaces, *Mater. Horiz.* 7 (2020) 2651–2661, <https://doi.org/10.1039/D0MH01344G>.
- [40] Z. Yuan, Z. Wan, Z. Tian, Y. Han, X. Huang, Y. Feng, W. Xie, X. Duan, S. Huang, X. Liu, J. Huang, In situ fused granular hydrogels with ultrastretchability, strong adhesion, and multi-bioactivities for efficient chronic wound care, *Chem. Eng. J.* 450 (2022) 138076, <https://doi.org/10.1016/j.cej.2022.138076>.
- [41] X. Zhao, D. Pei, Y. Yang, K. Xu, J. Yu, Y. Zhang, Q. Zhang, G. He, Y. Zhang, A. Li, et al., Green tea derivative driven smart hydrogels with desired functions for chronic diabetic wound treatment, *Adv. Funct. Mater.* 31 (2021) 2009442, <https://doi.org/10.1002/adfm.202009442>.
- [42] D. Li, K. Chen, H. Tang, S. Hu, L. Xin, X. Jing, Q. He, S. Wang, J. Song, L. Mei, et al., A logic-based diagnostic and therapeutic hydrogel with multistimuli responsiveness to orchestrate diabetic bone regeneration, *Adv. Mater.* 34 (2022) 2108430, <https://doi.org/10.1002/adma.202108430>.
- [43] Y. Qian, Y. Zheng, J. Jin, X. Wu, K. Xu, M. Dai, Q. Niu, H. Zheng, X. He, J. Shen, Immunoregulation in diabetic wound repair with a photoenhanced glycyrrhizic acid hydrogel scaffold, *Adv. Mater.* 34 (2022) 2200521, <https://doi.org/10.1002/adma.202200521>.
- [44] T.D. Schmittgen, K.J. Livak, Analyzing real-time PCR data by the comparative C-T method, *Nat. Protoc.* 3 (2008) 1101–1108, <https://doi.org/10.1038/nprot.2008.73>.
- [45] X. Su, W. Xie, P. Wang, Z. Tian, H. Wang, Z. Yuan, X. Liu, J. Huang, Strong underwater adhesion of injectable hydrogels triggered by diffusion of small molecules, *Mater. Horiz.* 8 (2021) 2199–2207, <https://doi.org/10.1039/D1MH00533B>.
- [46] D.A. Prystupa, A.M. Donald, Infrared study of gelatin conformations in the gel and sol states, *Polym. Gels Netw.* 4 (1996) 87–110, [https://doi.org/10.1016/0966-7822\(96\)00003-2](https://doi.org/10.1016/0966-7822(96)00003-2).
- [47] Z. Li, S.S. Percival, S. Bonard, L. Gu, Fabrication of nanoparticles using partially purified pomegranate ellagitannins and gelatin and their apoptotic effects, *Mol. Nutr. Food Res.* 55 (2011) 1096–1103, <https://doi.org/10.1002/mnfr.201000528>.
- [48] X. Gao, Z. Xu, G. Liu, J. Wu, Polyphenols as a versatile component in tissue engineering, *Acta Biomater.* 119 (2021) 57–74, <https://doi.org/10.1016/j.actbio.2020.11.004>.
- [49] Z. Wang, Y. Zhang, Y. Yin, J. Liu, P. Li, Y. Zhao, D. Bai, H. Zhao, X. Han, Q. Chen, High-strength and injectable supramolecular hydrogel self-assembled by monomeric nucleoside for tooth-extraction wound healing, *Adv. Mater.* 34 (2022) 2108300, <https://doi.org/10.1002/adma.202108300>.
- [50] S. Matoori, A. Veves, D.J. Mooney, Advanced bandages for diabetic wound healing, *Sci. Transl. Med.* 13 (2021) eabe4839, <https://doi.org/10.1126/scitranslmed.abe4839>.
- [51] L. Chavez-Galan, M.L. Olleros, D. Vesin, I. Garcia, Much more than M1 and M2 macrophages, there are also CD169(+) and TCR+ macrophages, *Front. Immunol.* 6 (2015) 263, <https://doi.org/10.3389/fimmu.2015.00263>.
- [52] M. Hesketh, K.B. Sahin, Z.E. West, R.Z. Murray, Macrophage phenotypes regulate scar formation and chronic wound healing, *Int. J. Mol. Sci.* 18 (2017) 1545, <https://doi.org/10.3390/ijms18071545>.
- [53] W. Gregg Edward, Y. Li, J. Wang, N. Rios Burrows, K. Ali Mohammed, D. Rolka, E. Williams Desmond, L. Geiss, Changes in diabetes-related complications in the United States, 1990–2010, *N. Engl. J. Med.* 370 (2014) 1514–1523, <https://doi.org/10.1056/NEJMoa1310799>.
- [54] G. Armstrong David, J.M. Boulton Andrew, A. Bus Sicco, Diabetic foot ulcers and their recurrence, *N. Engl. J. Med.* 376 (2017) 2367–2375, <https://doi.org/10.1056/NEJMra1615439>.
- [55] C. Zelen, D.G. Armstrong, 45-LB: results of a pilot evaluation of a novel autologous homologous skin construct treatment of diabetic foot wounds refractory to conventional treatments, *Diabetes* 68 (2019), <https://doi.org/10.2337/db19-45-LB>.
- [56] L.-H. Zhang, Q. Shen, Fully green poly(vinyl alcohol)/tea polyphenol composites and super anti-ultraviolet and -bacterial properties, *Macromol. Mater. Eng.* 305 (2020) 1900669, <https://doi.org/10.1002/mame.201900669>.
- [57] H.C. Oyeoka, C.M. Ewulonu, I.C. Nwuzor, C.M. Obele, J.T. Nwabanne, Packaging and degradability properties of polyvinyl alcohol/gelatin nanocomposite films filled water hyacinth cellulose nanocrystals, *Journal of Bioresources and Bioproducts* 6 (2021) 168–185, <https://doi.org/10.1016/j.jobab.2021.02.009>.
- [58] I. Zulkiflee, M.B. Fauzi, Gelatin-polyvinyl alcohol film for tissue engineering: a concise review, *Biomedicine* 9 (2021) 979, <https://doi.org/10.3390/biomedicine9080979>.